# Unconventional magnetic states and defects

Barts, Evgenii

*DOI:*
10.33612/diss.784926551

# Chapter 1

# Introduction

## 1.1 Advancements in magnetic memory devices by unconventional magnetic states

Magnetic memory is widely used in modern hard disk drives due to its robustness, high read-out speed and efficiency. In this type of memory, the information bits are stored in large stripe domains of magnetization that is either up or down. The idea of using cylindrical domains of flipped magnetization, known as magnetic bubbles, to store information bits was proposed and commercially implemented in the 1980s. However, magnetic bubbles were relatively large and could not replace conventional memory in data mass usage, primarily because they could not compete in prize with fast developments and scalability of semiconductor devices. Nevertheless, magnetic bubble memory devices are highly robust and are currently used in specific applications that require non-volatile memory in extreme conditions.

Magnetic Skyrmions are promising for new generations of magnetic memory devices due to their stability and mobility [1–3]. They are nano-sized emergent particles that behave like magnetic bubbles and are protected by topology [4], which means that they cannot be easily transformed into a collinear ferromagnetic state by local perturbations of spin directions. Skyrmions can be moved by a charge current, which makes them suitable for use in racetrack memory devices [5].

Non-collinear and non-coplanar antiferromagnets remain underexplored, although experimental evidence and theoretical proposals for unconventional magnetic orders and defects in these systems are exponentially growing [6–8]. The dimensionality and symmetry of the order parameter determine the topology of defects in ordered states of matter. As a result, a higher-dimensional parameter space describing non-collinear antiferromagnets makes topological defects in these materials more diverse and complex.

In this thesis, we study unconventional magnetic states and defects in realistic magnetic materials, such as magnetic bubbles in centrosymmetric ferromagnetic thin films and novel two- and three-dimensional topological defects in a non-collinear antiferromagnet. We also discuss spin interactions that can lead to unusual magnetic states. We calculate the bond-dependent Kitaev interactions in a van der Waals

ferromagnet. Finally, we explore the complex interplay between antiferromagnetic and ferrimagnetic states in the polar ferrimagnet, kamiokite, which gives rise to the electric polarization peaks in magnetization switching. This chapter introduces several concepts pertaining to non-collinear magnetism that are used throughout the thesis.

## 1.2 Topological defects in magnets

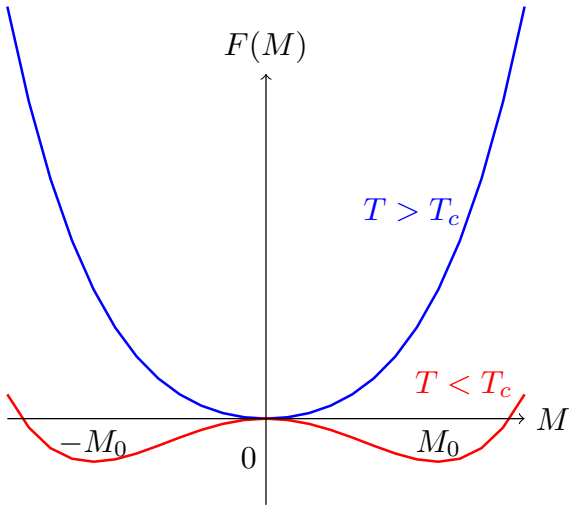


**Figure 1.1:** ***Landau free energy versus magnetization.*** *The blue curve shows the $M$-dependence at temperatures above critical temperature, and the red curve shows the $M$-dependence at temperatures below critical*

Concepts of *symmetry and topology* are important for description of ordered states of matter [4]. In spite of the rich variety of ordered states observed around us, symmetry-based phenomenological models of these states exhibit a remarkable *universality*. Symmetry breaking is a central idea of the theory developed by Landau to describe transitions between phases. For instance, in liquid water, all positions are equivalent, while ice is only invariant under shifts by a lattice constant of the crystal, which breaks the translational symmetry observed in the disordered state. Another example is the strong ferromagnetism in a piece of iron, which breaks rotational symmetry of the magnetization direction. In the high-temperature disordered state, the direction of local magnetization is arbitrary and averages out to zero total magnetization. In this case, the Landau expansion of the free energy describing the phase transition is

$$F(\boldsymbol{M}) = \frac{a\boldsymbol{M}^2}{2} + \frac{b\left(\boldsymbol{M}^2\right)^2}{4}, \tag{1.1}$$

where $a \sim (T - T_c)$ and $b$ are phenomenological parameters of the model, and $M$ is the absolute value of the vector order parameter $\boldsymbol{M} = M\boldsymbol{m}$, with the unit vector $\boldsymbol{m}$ describing its direction. In the high temperature disordered state, the minimum of free energy is at $M = 0$, since $a > 0$, whereas below the critical temperature ($T < T_c$, $a < 0$) the magnetization is non-zero $M^2 = -a/b$ (see Fig. 1.1), and its direction $\boldsymbol{m}$ is arbitrarily chosen, representing the spontaneous breaking of the rotational symmetry [9].

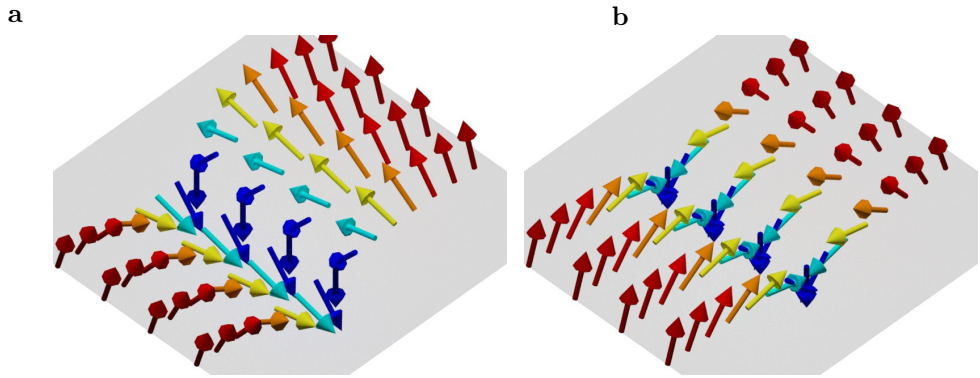


**Figure 1.2: Ferromagnetic domain walls**. *The two $\pi$ domain walls that separate spin-up and spin-down domains are of two types:* **a** *Bloch type, where the spins lie in the plane orthogonal to proliferation direction of the domain wall, and* **b** *Néel type, where the spins lie in the plane parallel to proliferation direction of the domain wall. If one of the type is allowed in the material, the two $\pi$ domain walls represent a 1D $2\pi$ topological soliton at the edge of the sample. These states are locally embedded in the uniform ground state. However, they also are found as periodically modulated* **a** *helical or* **b** *cycloidal spiral ground states.*

The concept of symmetry breaking explains many properties of an ordered state, making them strongly dependent on the dimensionality and geometrical structure of the order parameter space. Ginzburg-Landau theory provides a macroscopic description of superconductivity, where the free energy of the system depends on the order parameter represented by a complex number that describes the collective wave function of the superconducting system, i.e., the condensate of electron pairs in the microscopic BCS theory. This theory successfully predicted nearly all observable properties of superconductors, including the Meissner effect – the complete expulsion of the magnetic field from the superconductor.

In type II superconductors, a magnetic field can penetrate into the bulk superconductor in the form of cylindrical vertical domains, indicating a fundamentally different character of the phase transition to a normal metal in applied magnetic fields. These domains are quantized objects known as Abrikosov vortices. In the core of the vortex,

the superconductivity is suppressed, allowing the proliferation of magnetic field lines. This core represents a localized defect in the continuous order parameter space. Due to the continuity of the order parameter outside the core of the vortex, the phase of the order parameter must change over an integer number of $2\pi$ along a contour circumventing the vortex. This topological property of the vortex is independent of the contour.

Similar topological defects appear in different physical states that are described by order parameters with the same symmetry group. In a *one-dimensional* (1D) $XY$ spin model, non-singular $2\pi$-domain walls are similar to Abrikosov vortices, because the anisotropic planar spins are also described by a single phase that defines a vector pinned to the $xy$ coordinate plane. Figure 1.2 **a** shows such a soliton accumulating $2\pi$, which can be represented as a pair of two $\pi$-domain walls. Due to continuity, the total angle traced out by spins must be $2\pi Q_{\mathrm{TC}}^{(1D)}$, where $Q_{\mathrm{TC}}^{(1D)}$ is an integer number known as the winding number or topological charge of the defect. This property is topologically protected, since the integer $Q_{\mathrm{TC}}^{(1D)}$ can only change abruptly, making it robust against small fluctuations of the order parameter.

Properties and variety of topological defects strongly depend on geometrical structure of the order parameter space. Magnetic Skyrmions are topological states in systems of isotropic spins in *two spatial dimensions* (2D). These nano-sized topological defects are mobile and remarkably stable magnetic solitons [1, 2]. The robustness of the magnetic Skyrmion is due to topological protection [4], given that all possible spin directions are represented in its 2D swirling profile (see Fig. 1.3). The Skyrmion spin configuration wraps around the $xy$ plane in a way that it cannot be transformed into a collinear ferromagnetic state by local perturbations of spin directions. The topological charge measures the winding number,

$$Q_{\mathrm{TC}}^{(2D)} = \frac{1}{4\pi} \int d^2\boldsymbol{x}\, \boldsymbol{m} \cdot \left( \frac{\boldsymbol{m}}{\partial x} \times \frac{\boldsymbol{m}}{\partial y} \right), \tag{1.2}$$

where $\boldsymbol{m}$ is the unit vector along the magnetization. A magnetic bubble with $Q_{\mathrm{TC}}^{(2D)} = 1$ is an example of Skyrmion. The Skyrmion configuration in terms of azimuthal $\Phi$ and polar $\theta$ angles of the vector $\boldsymbol{m}$ in polar coordinates, $\boldsymbol{r} = (r\cos\phi, r\sin\phi)$, is given by

$$\theta(r,\phi) = \theta(r), \quad \Phi(r,\phi) = v\phi + \chi, \tag{1.3}$$

where the radial dependence $\theta(r)$ is determined by spin interactions and is obtained by minimizing the energy, $v$ is vorticity, and $\chi$ is helicity of the Skyrmion. Its topological charge is

$$Q_{\mathrm{TC}}^{(2D)} = \frac{1}{4\pi} \int_0^\infty dr \frac{\partial\theta}{\partial r} \sin\theta \int_0^{2\pi} d\phi\, \frac{\partial\Phi}{\partial\phi} = pv, \tag{1.4}$$

where $p = \frac{1}{2}\left(\cos\theta(r=0) - \cos\theta(r=\infty)\right)$ is the Skyrmion polarity. Note that the Skyrmion charge does not depend on $\chi$. The value of $\chi$ is typically pinned by magnetic

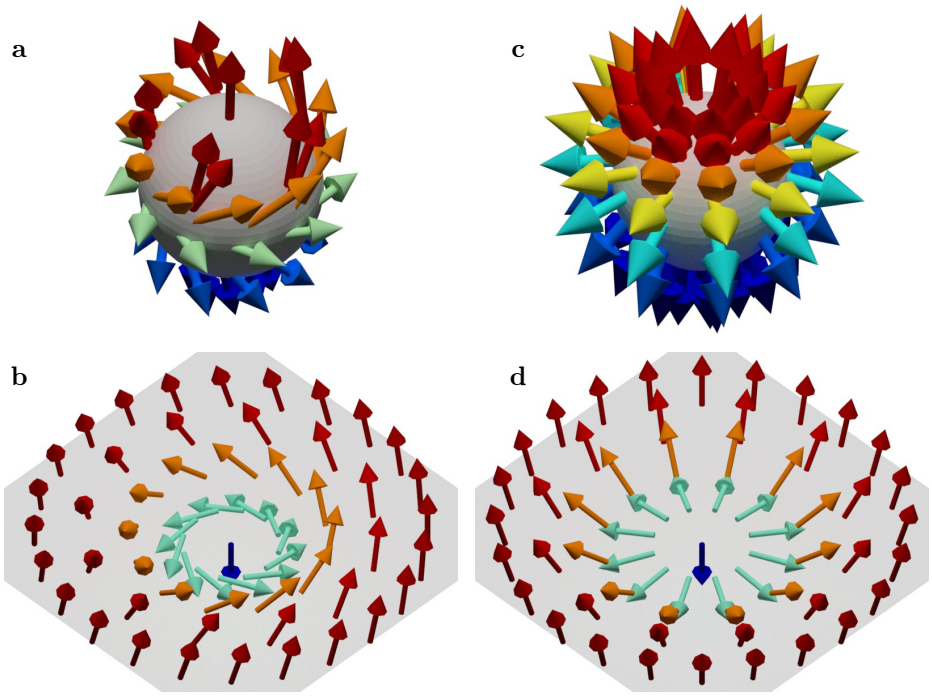


**Figure 1.3: 2D ferromagnetic Skyrmions: a** *Stereographic projection of the Bloch-type Skyrmion real-space configuration, shown in panel* **b**. *Arrows represent the direction of the local magnetization.* **c** *Stereographic projection of the Néel-type Skyrmion, shown in panel* **d**.

interactions leading to Bloch ($\chi = 0$) or Néel ($\chi = \pm\pi/2$) Skyrmions. Their real space configurations are shown in Fig. 1.3 **b** and **d** panels, respectively.

Magnetic Skyrmions, sometimes called baby-Skyrmions, are two-dimensional analogs of the original Skyrmion in three spatial dimensions introduced by T.H.R. Skyrme, who suggested that baryons, such as protons and neutrons, are topological solitons in a non-linear meson theory with a three-dimensional order parameter space (see Fig. 1.4 **a**) [10]. A similar topological defect, Shankar monopole, was predicted to exist in superfluid $^3$He A-phase [11, 12]. The realization of a three-dimensional order parameter in magnets would allow for a wealth of unusual states discussed in the context of superfluid $^3$He and nuclear physics. Related 3D defects, the so-called Hopf solitons (see Fig. 1.4 **b**) [13], were experimentally found in liquid crystals [14–19], Bose-Einstein condensate [20] and magnetic multilayers [21]. They were also theoretically predicted in ferromagnetic chiral magnets [22–27] and ferroelectrics [28].

The natural mathematical framework to describe topological defects is known as

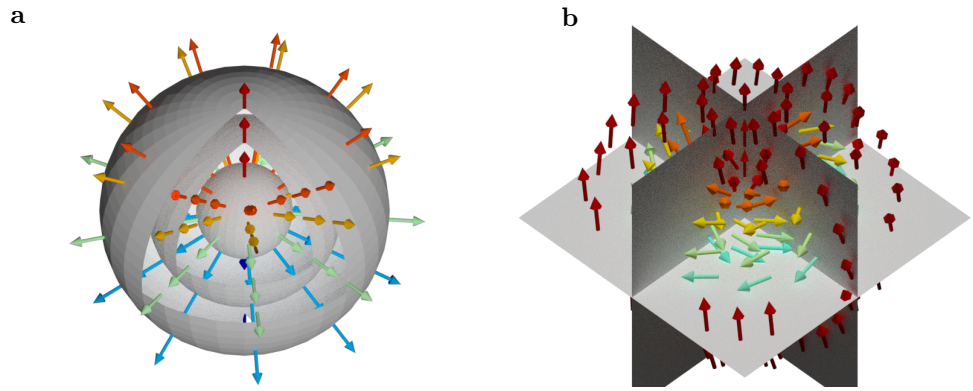


**Figure 1.4: 3D topological defects.** **a** *3D Skyrmion in the $SU(2)$ parameter space, described by the unitary matrix $U = e^{i\alpha(\boldsymbol{n}\cdot\boldsymbol{\sigma})}$. Arrows show the radial profile of $\boldsymbol{n}$, and $\alpha$ varies from 0 to $\pi$, as the radius varies from from zero to infinity, represented by the set of spheres.* **b** *Magnetic Hopfion with arrows showing the direction of the vector in the $S_2$ order parameter space.*

*homotopy theory*. To illustrate this concept, we consider the $2\pi$ domain wall for planar spins in the $XY$ model:

$$\boldsymbol{S}(x) = (\cos\alpha, \sin\alpha, 0), \text{ with } \quad \alpha(x) = \pi\left(\tanh(x/R) + 1\right). \tag{1.5}$$

We assume periodic boundary condition compactifying the 1D spin chain to a circle ($\mathbb{R}^1 \to S^1$). The function $\boldsymbol{S}(x)$ is a mapping from the circle (1D sphere) to the space of all spin directions, which for in-plane spins is also a circle, and the parameter $R$ determines the width of the domain wall. Solutions with different widths $R_1$ and $R_2$ are said to be *homotopically equivalent*, as they can be connected by a continuous deformation called homotopy. All domain wall solutions, parametrized by $R$, are connected by coordinate rescaling and, therefore, belong to the same homotopy class, described by the topological number $Q = 1$. On the other hand, the fully polarized state belongs to the topologically trivial class.

Homotopy groups provide a way to find and classify all topologically non-trivial mappings. The most used ones are the homotopy groups of spheres:

$$\pi_1(S^1) = \pi_2(S^2) = \pi_3(S^3) = \mathbb{Z}, \tag{1.6}$$

with $\pi_m(S^n) : \mathrm{Hom}(S^m \to S^n)$, describing mappings of $m$-dimensional sphere of the compactified coordinate space to the order parameter defined on $n$-dimensional sphere. We can now revisit the topological solitons mentioned above: $\pi_1(S^1)$ classifies domain walls in spin chains and 2D Abrikosov vortices in superconductors; $\pi_2(S^2)$ and $\pi_3(S^3)$

describe 2D and 3D Skyrmions, respectively. The homotopies form an additive group of integer numbers $\mathbb{Z}$ that gives a useful physical intuition, e.g., topological charge of the two $2\pi$ domain walls is $Q_{\rm TC}^{(1D)} = 2$ and two walls with opposite topological charges can be continuously deformed to the trivial uniform state, i.e., they become annihilated in the deformation process.

### 1.2.1 Topological solitons in three dimensions

Clarifying similarities (and also fundamental differences) between the aforementioned three-dimensional topological defects is of high importance for their detection and manipulation in real materials. The deep connection between the $SU(2)$ Skyrmion as a nucleon constructed of scalar mesons, the Shankar $SO(3)$ soliton in superfluid $^3$He and the Hopfion in ferromagnets ($S^2$ order parameter space) is that they can be classified by the same topological index [29, 30]:

$$\pi_3(S^3) = \pi_3(SU(2)) = \pi_3(SO(3)) = \pi_3(S^2) = \mathbb{Z}. \tag{1.7}$$

Here, we discuss the logic behind this equivalence. Consider the vector of four scalar fields $\Phi_\mu(\boldsymbol{r}) = (\Phi_0, \Phi_x, \Phi_y, \Phi_z)$, constrained to the 3-sphere $\left(\sum_{\mu=0}^{4} \Phi_\mu^2 = 1\right)$. These states can represent three light meson fields $(\pi_+, \pi_-, \pi_0)$ and an auxiliary field $\sigma = \sqrt{1 - \boldsymbol{\pi}^2}$. The degree of the $\Phi_\mu(\boldsymbol{r})$ mapping in the compactified three spatial dimensions is given by the wrapping number,

$$Q_{\rm TC}^{(3D)} = \frac{1}{12\pi^2} \int d^3x \, \varepsilon_{\alpha\beta\gamma\delta} \, \varepsilon_{ijk} \, \Phi_\alpha (\partial_i \Phi_\beta)(\partial_j \Phi_\gamma)(\partial_k \Phi_\delta), \tag{1.8}$$

where $\varepsilon_{ijk}$ and $\varepsilon_{\alpha\beta\gamma\delta}$ are the antisymmetric Levi-Civita tensors ($i, j, k = x, y$ or $z$ and $\alpha, \beta, \gamma, \delta = 0, x, y$ or $z$), and the summation over repeated indices is assumed. Here, we employed $Q_{\rm TC}^{(3D)} = \frac{\int_{S_3} d\Omega}{A_{S_3}}$, where $d\Omega$ is the solid angle spanned by the vector $\Phi_\mu(\boldsymbol{r})$ in the three dimensional space $S_3$, and $A_{S_3} = 2\pi^2$ is the $S_3$ surface area. The solid angle is expressed as

$$d\Omega = \frac{1}{6} \varepsilon_{\alpha\beta\gamma\delta} \, \varepsilon_{ijk} \, \Phi_\alpha (\partial_i \Phi_\beta)(\partial_j \Phi_\gamma)(\partial_k \Phi_\delta) \, dx \, dy \, dz. \tag{1.9}$$

The topological index $Q_{\rm TC}^{(3D)}$ is also the $SU(2)$ Skyrmion number, since the parameter spaces are isomorphic ($SU(2) = S_3$), which can be proved as follows:

$$U(\boldsymbol{r}) = \Phi_0 \mathbb{1} + i \boldsymbol{\Phi} \cdot \boldsymbol{\sigma} = \begin{pmatrix} \Phi_0 + i\Phi_z & \Phi_x - i\Phi_y \\ \Phi_x + i\Phi_y & \Phi_0 - i\Phi_z \end{pmatrix}, \tag{1.10}$$

where $\mathbb{1}$ is the $2 \times 2$ unit matrix and $\boldsymbol{\sigma} = (\sigma_x, \sigma_y, \sigma_z)$ is a vector composed of Pauli matrices. Thus, the Skyrmion number is obtained by writing Eq. (1.8) in terms of

$SU(2)$ matrices,

$$Q_{\mathrm{TC}}^{(3D)} = -\frac{1}{24\pi^2}\int d^3x\,\varepsilon_{ijk}\,\mathrm{tr}\big[L_iL_jL_k\big], \tag{1.11}$$

where $L_i = U^\dagger\partial_i U$. For $SO(3)$ order parameter space introduced by a rotation matrix $R$, the topological charge is

$$Q_{\mathrm{TC}}^{(3D)} = -\frac{1}{96\pi^2}\int d^3x\,\varepsilon_{ijk}\,\mathrm{tr}\big[I_iI_jI_k\big], \tag{1.12}$$

where $I_i = R^{-1}\partial_i R$. Even without Eq. (1.12), one can classify $SO(3)$ mappings using the $SU(2)$ topological index, by explicitly constructing mapping between $SO(3)$ and $SU(2)$ matrices:

$$R_{ab} = \frac{1}{2}\mathrm{tr}\left(\sigma_a U^\dagger\sigma_b U\right). \tag{1.13}$$

This equation defines the double-covering representation of $SO(3)$, since matrices $U$ and $-U$ lead to the same matrix $R$. In group theory, the $SO(3)$ group is equivalent to the coset space of the $SU(2)$:

$$SO(3) = SU(2)/\mathbb{Z}_2, \tag{1.14}$$

where $\mathbb{Z}_2 = \{+1, -1\}$, the two-element additive group. The coset space is also called fiber bundle, which has intuitive geometrical interpretation. Namely, $SU(2)$ is geometrically equivalent to the 3D sphere $S_3$ that can be cut by half by identifying antipodal points of the sphere in order to map it onto $SO(3)$. In this way, $SO(3)$ is a cap in the four-dimensional space with identified antipodal points at the edge. This non-trivial edge allows for topological vortices, due to existence of incontractible loops that cross the edge, classified by $\pi_1(SO(3)) = \mathbb{Z}_2$. Notably, such double-covering representations can be constructed using auxiliary gauge fields. We can introduce a $Z_2$ gauge field to enlarge the $SO(3)$ space to the $SU(2)$ space. However, since the topological index $Q_{\mathrm{TC}}^{(3D)}$ in Eq. (1.11) is gauge invariant (does not change under $U \to -U$), one can use directly $Q_{\mathrm{TC}}^{(3D)}$ to classify $SO(3)$ mappings.

Similarly, gauge degrees of freedom allow to find the correspondence between the 3D Skyrmion charge and the Hopf index for a unit vector $\boldsymbol{n}$ tracing out the $S_2$ sphere. The vectorial order parameter can be expressed as a coset space

$$S_2 = SO(3)/U(1), \tag{1.15}$$

This truncation can be introduced by defining the $SO(3)$ matrix as,

$$R = (\boldsymbol{V}_1, \boldsymbol{V}_2, \boldsymbol{n}), \tag{1.16}$$

where columns are the unit vectors $\boldsymbol{V}_1, \boldsymbol{V}_2, \boldsymbol{n}$ that form the right-handed basis, $[\boldsymbol{V}_1 \times \boldsymbol{V}_2] = \boldsymbol{n}$. For $S_2$ order parameter space, the gauge degree of freedom is an angle

$\psi$, since the vectors $\boldsymbol{V}_{1,2}$ can be rotated about the vector $\boldsymbol{n}$ by the angle $\psi$ without changing the vector $\boldsymbol{n}$. In this gauge field formalism, the 3D topological charge is equivalent to the Hopf index given by

$$\mathcal{H} = -\frac{1}{16\pi^2}\int d^3x\,(\mathbf{a}\cdot\mathbf{b}), \tag{1.17}$$

where $\boldsymbol{a} = \sum_{i=x,y,z} V_1^i \boldsymbol{\partial} V_2^i$ and the corresponding magnetic field $\mathbf{b} = [\nabla \times \mathbf{a}]$ [29, 31]. Since only gauge-invariant quantities are observable, one can use $Q_{\mathrm{TC}}^{(3D)}$ to classify 3D topological states with the $S_2$ order parameter space. The fundamental difference between the $S_2$ Hopfion and $SU(2)$ or $SO(3)$ solitons is the different dimensionality of the parameter spaces, corresponding to different physical realizations.

### 1.2.2 3D Skyrmion charge

Here we present the formal equivalence between topological indices in Eq. (1.7). We show that instead of using the mapping to 3-sphere (see Eq. (1.11)), one can calculate topological charge directly by substituting $I_i$ in Eq. (1.12) with $R^{-1}\partial_i R$, where $R \in \mathrm{SO}(3)$ is

$$R = R_z(\phi)R_y(\theta)R_z(\Psi), \tag{1.18}$$

where $R_z$ and $R_y$ are the matrices of rotations around the $z$ and $y$ axes. We use

$$L_i = R^{-1}\partial_i R = \sum_a A_i^a S^a \tag{1.19}$$

where $S^a$ $(a = x, y, z)$ are generators of rotations around the three axes:

$$S^x = \begin{pmatrix} 0 & 0 & 0 \\ 0 & 0 & -1 \\ 0 & 1 & 0 \end{pmatrix} \; S^y = \begin{pmatrix} 0 & 0 & 1 \\ 0 & 0 & 0 \\ -1 & 0 & 0 \end{pmatrix} \; S^z = \begin{pmatrix} 0 & -1 & 0 \\ 1 & 0 & 0 \\ 0 & 0 & 0 \end{pmatrix} \tag{1.20}$$

satisfying

$$\left[S^a, S^b\right] = \varepsilon^{abc} S^c \quad tr\left(S^a S^b\right) = -2\delta^{ab} \quad \mathrm{tr}\left(S^a S^b S^c\right) = -\varepsilon^{abc} \tag{1.21}$$

Equation (1.12) in the main text can then be written in the form

$$\mathcal{H} = \frac{1}{16\pi^2}\int d^3x\, \varepsilon_{ijk}\, A_i^x A_j^y A_k^z \tag{1.22}$$

Substituting the expressions for the expansion coefficients

$$\begin{aligned} A_i^x &= \sin\psi\,\partial_i\theta - \cos\psi\sin\theta\,\partial_i\phi \\ A_i^y &= \cos\psi\,\partial_i\theta + \sin\psi\sin\theta\,\partial_i\phi \\ A_i^z &= \cos\theta\,\partial_i\phi - \partial_i\psi \end{aligned} \tag{1.23}$$

we obtain

$$\mathcal{H} = \frac{1}{16\pi^2} \int d^3x \, \varepsilon_{ijk} \, \partial_i\theta \, \sin\theta \, \partial_j\phi \, \partial_k\psi \tag{1.24}$$

The same expression is obtained by substituting $a_i = \mathbf{V}_1 \cdot \partial_i \mathbf{V}_2 = -D_i\psi = -\partial_i\psi - \cos\theta\partial_i\phi$ into Eq. (1.17) in the main text. Although the Lie algebras $su(2)$ and $so(3)$ are isomorphic to each other, the topological indices have prefactors in front of the integrals for $SU(2)$ and $SO(3)$ groups. This is related to the fact that the generators $S^a$ have to be rescaled in order to build up the isomorphism:

$$S^a = \frac{-i}{2}\sigma^a, \tag{1.25}$$

where $\sigma^a$ is the vector of Pauli matrices.

## 1.3 Magnetostatics of magnetic bubbles in thin films

Nontrivial topology by itself does not ensure stability of defects against collapse or infinite expansion. Therefore, stable defects require a competition between interactions that tend to expand and shrink the defect. In this section, we show how an array of Skyrmions can be stabilized by magnetostatic interactions in ferromagnetic thin films.

The magnetization in a ferromagnetic thin film generates demagnetization fields, $\boldsymbol{H}_d$, as follows from the Maxwell equation,

$$\boldsymbol{\nabla} \cdot \boldsymbol{B} = \boldsymbol{\nabla} \cdot (\boldsymbol{H}_{\rm d} + \boldsymbol{H}_{\rm ext} + 4\pi\boldsymbol{M}) = 0, \tag{1.26}$$

$\boldsymbol{H}_{\rm ext}$ being an external applied field. It is the magnetic analog of Gauss law in electrostatics. Thus, the inhomogeneous magnetization gives rise to a magnetic charge density,

$$\rho_m = -\nabla\boldsymbol{M}. \tag{1.27}$$

Interactions between the magnetic charges are described by the magnetostatic energy (see [32, 33] for details),

$$E_{\rm ms} = \frac{1}{2} \int d^3x_1 \, d^3x_2 \frac{\rho_m(\boldsymbol{x}_1)\rho_m(\boldsymbol{x}_2)}{|\boldsymbol{x}_1 - \boldsymbol{x}_2|}. \tag{1.28}$$

The energy can be written through the demagnetization fields density in Eq. (1.26) using integration by parts,

$$E_{\rm ms} = \frac{1}{8\pi} \int d^3x \, \boldsymbol{H}_{\rm d}^2(\boldsymbol{x}) = -\frac{1}{2} \int d^3x \, \boldsymbol{M}(\boldsymbol{x}) \cdot \boldsymbol{H}_{\rm d}(\boldsymbol{x}). \tag{1.29}$$

This interaction is difficult to work with due to its long-range character. However, the magnetostatic energy density becomes local in the momentum space, if the

magnetization only varies in the film plane: $\boldsymbol{M} = \boldsymbol{M}(x, y)$ [34],

$$E_{\rm ms} = 2\pi h S \sum_{\boldsymbol{q}} \left[ f(qh)|M^z_{\boldsymbol{q}}|^2 + (1 - f(qh))|\hat{\boldsymbol{q}} \cdot \boldsymbol{M}_{\boldsymbol{q}}|^2 \right], \tag{1.30}$$

where $h$ and $S$ are, respectively, the film thickness and area, $\hat{\boldsymbol{q}} = \frac{\boldsymbol{q}}{q}$, $f(x) = \frac{1-e^{-x}}{x}$ and $\boldsymbol{M}_{\boldsymbol{q}}$ is the Fourier transformation of the magnetization,

$$\boldsymbol{M}_{\boldsymbol{q}} = \frac{1}{S} \int d^2x \, e^{-i\boldsymbol{q}\cdot\boldsymbol{x}} \, \boldsymbol{M}(\boldsymbol{x}). \tag{1.31}$$

We can derive the expression for the magnetostatic energy in Eq. (1.30) in the reciprocal space for the magnetization distribution

$$\boldsymbol{M}(\boldsymbol{x}) = (\theta(h - z) - \theta(-z)) \, \boldsymbol{M}(x, y), \tag{1.32}$$

which induces effective magnetic charges,

$$\rho(\boldsymbol{x}) = -\boldsymbol{\nabla} \cdot \boldsymbol{M} = -\left(\theta(h - z) - \theta(-z)\right) \boldsymbol{\nabla}_{\parallel} \cdot \boldsymbol{M} + \left(\delta(h - z) - \delta(z)\right) M^z, \tag{1.33}$$

In the reciprocal space,

$$\rho_{\boldsymbol{q}} = \int \frac{d^3x}{Sh} \rho(\boldsymbol{x}) e^{-i\boldsymbol{q}\cdot\boldsymbol{x}} = \left( \frac{\boldsymbol{q}_{\parallel} \cdot \boldsymbol{M}_{\boldsymbol{q}}}{q_z h} + \frac{M^z_{\boldsymbol{q}}}{h} \right) \left( e^{-iq_z h} - 1 \right), \tag{1.34}$$

where the first (second) term describes bulk (surface) induced magnetic charges, and $S$ and $h$ is the film area and thickness. The magnetostatic energy can then be written in the form,

$$E_{\rm ms} = 2\pi S h \sum_{\boldsymbol{q}_{\parallel}, q_z} \frac{\rho_{\boldsymbol{q}} \rho_{-\boldsymbol{q}}}{\boldsymbol{q}^2_{\parallel} + q^2_z}, \tag{1.35}$$

where we used Fourier transform of the Coulomb potential,

$$\int d\boldsymbol{r} \frac{e^{i\boldsymbol{q}\cdot\boldsymbol{r}}}{r} = \frac{4\pi}{q^2}. \tag{1.36}$$

Replacing the sum over $q_z$ by the integral $\left( \sum_{q_z} = \int \frac{dq_z h}{2\pi} \right)$, we can rewrite the magnetostatic energy in the simple form,

$$E_{\rm ms} = 2\pi S h \sum_{\boldsymbol{q}_{\parallel}} \left( (f(0) - f(q_{\parallel} h))(\hat{\boldsymbol{q}}_{\parallel} \cdot \boldsymbol{M}_{\boldsymbol{q}})^2 + f(q_{\parallel} h)(M^z_{\boldsymbol{q}})^2 \right), \tag{1.37}$$

with

$$f(x) = \int_{-\infty}^{\infty} \frac{dt}{\pi} \frac{\left(1 - e^{-it}\right)}{t^2 + x^2} = \frac{1 - e^{-x}}{x}. \tag{1.38}$$

The first term in Eq. (1.30) stems from the surface magnetic charges resulting from a discontinuous jump in the $z$ component of the magnetization. In the case of a homogeneous magnetization direction, the energy density $\mathcal{E}_{\rm ms} = 2\pi M_z^2$ favors an in-plane magnetization, which may be in conflict with the uniaxial magnetic anisotropy favoring the out-of-plane direction, $-\frac{1}{2}K_1 M_z^2$ with $K_1 > 0$. The so-called quality factor $Q = \frac{K_1}{4\pi}$ measures the relative strength of the magnetic anisotropy and magnetostatic interactions: for $Q < 1$ the magnetization lies in the film plane, whereas for $Q > 1$ an out-of-plane direction is preferred. In the latter case, the ground state in zero magnetic field consists of stripes of alternating spin-up and spin-down domains. Such a state is energetically favorable since the demagnetization field lines are closed in the vicinity of two neighboring domains (see Fig. 1.5 **a**) rather than spread over a large volume around the material. The spatial modulation of the magnetization favored by magnetostatic interactions is described by the $q$-dependence of the magnetostatic energy, which decreases linearly with $q$: $f(x) \approx 1 - \frac{x}{2}$, for small $x = qh$. The second term in Eq. (1.30) originates from the bulk magnetic charges. Being always positive, it favors the magnetization orthogonal to the wave vector $\boldsymbol{q}$. This condition is satisfied for domain walls of Bloch type and helical spiral states (see Fig. 1.2 **a**).

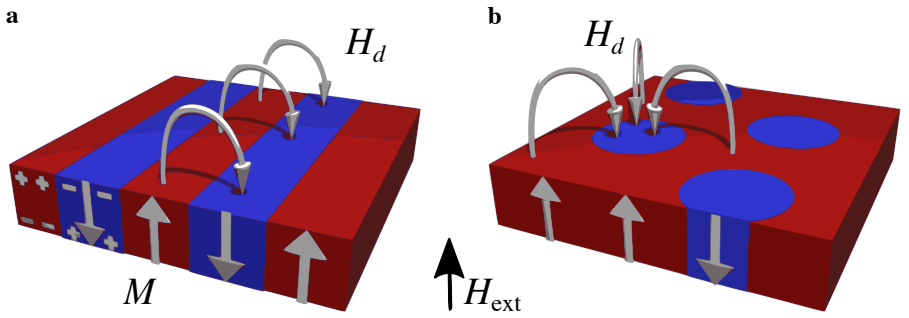


**Figure 1.5:** ***Magnetic ground states in a thin film in the Ising model.*** **a** *Stripe up- (red color) and down- (blue color) magnetization domains ($\boldsymbol{M}$) is the ground state for a ferromagnetic thin film. Under magnetic fields applied perpendicular to the plane ($\mathbf{H}_{\rm ext}$), the state deforms to* **b** *the hexagonal bubbles array and eventually becomes the fully polarized uniform state (not shown here). Thick white arrows show demagnetization field lines ($\mathbf{H}_{\rm d}$) and $\pm$ signs indicate the distribution of the surface magnetic charges.*

When an external magnetic field is applied along the vertical $z$ direction, domains with magnetization along the field start growing in size. At some critical field, the system undergoes a phase transition to a hexagonal lattice of cylindrical domains (see Fig. 1.5 **b**), known as magnetic bubbles. The magnetic bubble array is more efficient

at gaining the Zeeman interaction energy than the stripe-domain state, as was shown by Garel and Doniach for Ising spins [35]. This stabilization mechanism is present in many physical phenomena and can be understood within Landau theory. In reciprocal space, one of the quartic terms of $b\left(\boldsymbol{M}^2(\boldsymbol{r})\right)^2$ has the form

$$b\sum_{\boldsymbol{q},\boldsymbol{k},\boldsymbol{p}}(\boldsymbol{M}_0\cdot\boldsymbol{M}_{\boldsymbol{q}})(\boldsymbol{M}_{\boldsymbol{k}}\cdot\boldsymbol{M}_{\boldsymbol{p}})\delta_{\boldsymbol{q}+\boldsymbol{k}+\boldsymbol{p}}, \tag{1.39}$$

in which $\boldsymbol{M}_0$ is a large average magnetization induced by the applied field. This interaction favors the superposition of the uniform state and the three-spiral state with the 120° angle between the wave vectors [36, 37],

$$\boldsymbol{M}(\boldsymbol{r}) = \boldsymbol{M}_0 + \sum_{i=1,2,3} M_h\left(\boldsymbol{n}_{1,i}\cos(\boldsymbol{q}_i\cdot\boldsymbol{r}+\phi_i) + \boldsymbol{n}_{2,i}\sin(\boldsymbol{q}_i\cdot\boldsymbol{r}+\phi_i)\right), \tag{1.40}$$

which is nothing but the hexagonal arrays of magnetic bubbles (we neglect small higher harmonics). Here, $M_h$ is the spiral amplitude and the orthogonal vectors $\boldsymbol{n}_{1,i}\perp\boldsymbol{n}_{2,i}$ define spiral plane orthogonal to the wave vector $\boldsymbol{q}_i$ in the case of helical spirals. The spiral phases $\phi_i$ are adjusted to obtain a negative energy contribution in Eq. (1.39): $\phi_1+\phi_2+\phi_3=\pi$. This phase-locking gives rise to a non-zero total topological charge of the skyrmion crystal.

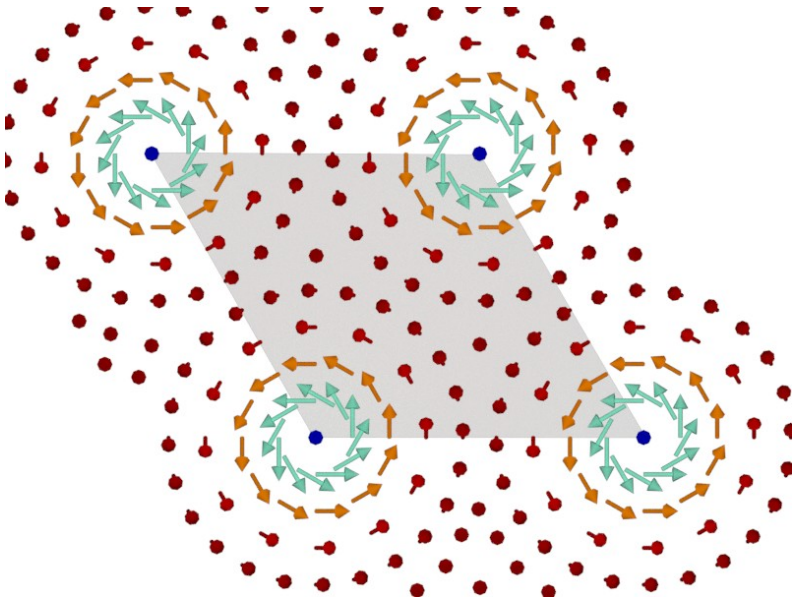

**Figure 1.6:** ***Bloch-type Skyrmion crystal.*** *The grey-shaded area represents the magnetic unit cell of the Skyrmion crystal.*

## 1.4 Chiral and achiral interactions favoring non-collinear spin orders

Next we discuss stabilization mechanisms of non-collinear spins states in chiral and achiral magnets. Skyrmions have been found in many chiral magnets, wherein inversion symmetry breaking allows for an antisymmetric spin interaction that stabilizes non-collinear spin textures. The continuum model of a chiral magnet in two dimensions is

$$E_{\text{chiral}} = E_{\text{ex}} + E_{\text{LI}} + E_{\text{a}}, \tag{1.41}$$

where the first term is the spin-stiffness energy,

$$E_{\text{ex}} = \frac{c}{2} \int d^2x \sum_{\mu=x,y} \left(\partial_i \boldsymbol{S}\right)^2, \tag{1.42}$$

which originates from ferromagnetic exchange interactions $-J \sum_{<i,j>} \boldsymbol{S}_i \cdot \boldsymbol{S}_j$ giving an energy penalty for large angles between spins, and $c$ ($\sim J$) is the spin stiffness constant. Other terms in Eq. (1.41) are anisotropic energy corrections resulting from the relativistic spin-orbit coupling; and their form strongly depends on the crystal symmetries. The second term in Eq. (1.41) is the so-called Lifshitz invariant

$$E_{\text{LI}} = \alpha_{\text{LI}} \int d^2x \left(S^a \partial_\mu S^b - S^b \partial_\mu S^a\right), \tag{1.43}$$

$a, b$ label spin components and $\mu$ is an in-plane direction. It originates from antisymmetric Dzyaloshinskii-Moriya exchange interactions (DMI) [38, 39]

$$D \sum_{<i,j>} \left(S_i^a S_j^b - S_i^b S_j^a\right) \tag{1.44}$$

with $D \sim \alpha_{\text{LI}} a$, where $\alpha_{\text{LI}}$ is the strength of the anisotropic Lifshitz term introduced in Eq. (1.43) and $a$ is the lattice constant. The last term in Eq. (1.41) represents spatially uniform anisotropic interactions including intrinsic single-ion anisotropy and Zeeman interaction with applied field, $\boldsymbol{H}$: $E_{\text{Z}} = \int d^2x \left(-\boldsymbol{M} \cdot \boldsymbol{H}\right)$. For crystal symmetry groups with a preferred axis, such as in tetragonal crystals, the single-ion anisotropy is $E_{\text{si}} = -K_2 \int d^2x \, S_z^2$, whereas for cubic magnets, $E_{\text{si}} = -K_4 \int d^2x \left(S_x^4 + S_y^4 + S_z^4\right)$.

Stabilization of an isolated Skyrmion can be explained by dimensional analysis. For a localized spin texture to be stable, its energy should have a minimum as the function of $R$, which represents the characteristic size of the localized state. The Skyrmion energy scales with $R$ as

$$E_{\text{chiral}}(R) = A_{\text{ex}} - D A_{\text{DM}} R + K_2 A_{\text{a}} R^2, \tag{1.45}$$

where $A_{\rm ex}$, $A_{\rm DM}$ and $A_{\rm a}$ are some positive constants. The energy has the minimum at $R_{\rm chiral} = \frac{DA_{\rm DM}}{2K_2A_{\rm a}}$ allowing for a finite size spin texture.

Skyrmions stabilized by DMI can form stable crystals as described by Eq. (1.40), similar to magnetic bubble arrays stabilized by the magnetostatic energy. In the momentum space, the exchange energy is quadratic function of the modulation vector $q$ and the DMI is linear in $q$, which leads to a spin modulation with $q = D/J$. The energy decrease due to the modulation is proportional to $-D^2/J$, which is quadratic in the SOC ($\lambda$) since $D \sim \lambda$, and should be compared to the increase in the anisotropic energy ($K_2 \sim \lambda^2$). Spin spirals and Skyrmion crystals are often found in cubic materials with the relatively low anisotropy ($K_4 \sim \lambda^4$). Usually $D/J \ll 1$, since DMI is the relativistic energy correction, which makes the period of magnetic modulations in chiral magnets much larger than the lattice constant.

Frustrated magnets can have a centrosymmetric lattice and yet host non-collinear spin textures. Competing exchange interactions result in frustration of uniform magnetic orders in these materials. An example is a triangular lattice with nearest-neighbor ferromagnetic interaction and next-nearest-neighbor antiferromagnetic interaction, which was predicted to host a plethora of modulated states, including Skyrmion crystals for non-zero [40] and zero temperatures [41]. The formation of non-collinear states can be verified by considering a continuum model

$$E_{\rm achiral} = E_{\rm ex} + E_{\rm ex4} + E_{\rm a}, \tag{1.46}$$

which differs from Eq. (1.41) by $E_{\rm ex4}$ replacing DMI. This term originating from frustration is proportional to the second power of the second derivative of spin,

$$E_{\rm ex4} = \frac{c_4}{4}\int d^2x \sum_{\mu=x,y} \left(\partial_i^2 \boldsymbol{S}\right)^2. \tag{1.47}$$

Then the scaling for an individual Skyrmion is modified to

$$E_{\rm achiral}(R) = A_{\rm ex} + \frac{c_4}{R^2}A_{\rm ex4} + K_2A_{\rm a}R^2, \tag{1.48}$$

with the energy minimum at $R_{\rm achiral} = \left(\frac{c_4A_{\rm ex4}}{K_2A_{\rm a}}\right)^{\frac{1}{4}}$. In this case, non-zero $c_4$ prevents the defect from collapsing.

The other difference is that the term proportional to the second power of the first derivative ($E_{\rm ex}$) has a negative coefficient, which is why term $E_{\rm ex4}$ has to be added. Spin-spiral states with the modulation wavevector $q = \sqrt{|c|/c_4}$ are formed due to instability of the uniform ferromagnetic state with $c < 0$, beyond the so-called Lifshitz point ($c = 0$) [41, 42]. Notably, the continuum limit is not always accurate for frustrated magnets, since the competing exchange interactions can be of the same order of magnitude, and there is no clear separation of length scales, as

for chiral magnets. An example is a short-range spiral state ($\sim 7$ lattice constants) due to the interplane frustrated exchange interactions found in iron-based langasites (see Chapter 3). Tiny Skyrmions of a few nanometers in size were observed in metallic centrosymmetric magnets: triangular $Gd_2PdSi_3$ [43], hexagonal kagomé $Gd_3Ru_4Al_{12}$ [44], and tetragonal $GdRu_2Si_2$ [45]. Peculiar $4q$ spiral hedgehog nanomodulations were observed in cubic $SrFeO_3$ [46, 47]. Small-wavelength modulations $q \sim 2\pi/a$ strongly affect conduction electrons since $q \sim k_F \sim 2\pi/a$ in metallic magnetic systems. Unconventional non-collinear orders with large intrinsic topological Hall response were predicted in Double-Exchange (or Kondo-Lattice) models [48, 49]. The comprehensive review of mechanisms of itinerant frustration can be found in Ref. [50].

In three spatial dimensions (3D), the energies get an extra power of $R$ under the scaling transformation from the additional integration over $z$. For the achiral magnet, the energy in Eq (1.48) is modified to

$$E^{3D}_{\text{achiral}}(R) = cA_{\text{ex}}R + \frac{c_4}{R}A_{\text{ex4}} + K_2A_{\text{a}}R^3, \tag{1.49}$$

which has the minimum at

$$R^{3D}_{\text{achiral}} = \frac{-cA_{\text{ex}} + \sqrt{(cA_{\text{ex}})^2 + 12K_2A_{\text{a}}c_4A_{\text{ex4}}}}{6K_2A_{\text{a}}}. \tag{1.50}$$

The solution always exists unless the Skyrmion is comparable with the lattice spacing, in which case the continuum limit is not applicable. In absence of frustration, the terms of fourth order in gradients of spin are relatively small, unless the size of the magnetic defect is as small as one lattice constant. For isotropic systems $K_2 = 0$, the energy minimum is at $R^{3D}_{\text{achiral}} = \frac{c_4A_{\text{ex4}}}{cA_{\text{ex}}}$. The energy proportional to the fourth power of derivatives of meson fields was used by Skyrme to prevent the collapse of the original 3D Skyrmions [10].

The energy of the chiral magnet in 3D scales as

$$E^{3D}_{\text{chiral}}(R) = cE_{\text{ex}}R - DA_{\text{DM}}R^2 + K_2A_{\text{a}}R^3, \tag{1.51}$$

with the minimum at

$$R^{3D}_{\text{chiral}} = \frac{DA_{\text{DM}} + \sqrt{(DA_{\text{DM}})^2 - 3K_2A_{\text{a}}cA_{\text{ex}}}}{3K_2A_{\text{a}}}. \tag{1.52}$$

It shows that DMI can stabilize 3D topological defects. In practice, the magnitude of DM constant is limited by the critical value, at which DMI causes the instability of the homogeneous ground state toward the formation of a spiral state.

More accurately, stabilization of an isolated soliton can be understood by the scaling analysis of its energy [51]. A stable localized spin texture must have an energy minimum under the rescaling transformation, $\boldsymbol{x} \to \Lambda\boldsymbol{x}$: $\frac{dE[S(\Lambda\boldsymbol{x})]}{d\Lambda}\Big|_{\text{at }\Lambda=1} = 0$. This gives an energy balance condition for the soliton stability.

Using this argument in a chiral layered material, DM interactions with only in-plane spatial derivatives can, in principle, stabilize a 3D topological defect. The scaling analysis needs to be considered separately for the in- and out-of-plane directions. The crystal symmetry implies that such a defect is axially symmetric. Its stability under the scaling transformations along the $z$ and radial directions implies that

$$\begin{cases} E_{\rm ex}^{(z)} = E_{\rm ex}^{(xy)} + E_{\rm DM} + E_{\rm a}, \\ \\ E_{\rm DM} + 2(E_{\rm ex}^{(z)} + E_{\rm a}) = 0, \end{cases} \tag{1.53}$$

where $E_{\rm ex}^{(z)}$ and $E_{\rm ex}^{(xy)}$ are, respectively, the interlayer and intralayer exchange energies, $E_{\rm DM}$ is the Lifshitz invariant energy and $E_{\rm a}$ is the energy of the remaining anisotropy terms. From Eq. (1.53) we obtain, $2E_{\rm ex}^{(xy)} + 3E_{\rm DM} + 4E_{\rm a} = 0$, where $E_{\rm DM} < 0$ and $E_{\rm ex}^{(xy)}, E_{\rm a} > 0$ (the anisotropy energy $E_{\rm a}$ is counted from the energy of the uniform state with $\boldsymbol{n} \| z$). Although the DMI energy only involves in-plane derivatives of the order parameter, it can make the defect stable both in the radial and $z$ directions provided

$$\frac{2}{3} E_{\rm ex}^{(xy)} < |E_{\rm DM}| < 2E_{\rm ex}^{(xy)}, \tag{1.54}$$

where the first inequality results from $E_{\rm a} > 0$, and the second inequality ensures that the total energy of the defect is positive.

## 1.5 Microscopic origin of magnetic interactions

In insulators, the virtual electron delocalization leads to interactions between spins of electrons localized on ionic sites [52]. In this section, we explore different mechanisms that give rise to isotropic and anisotropic spin interactions.

### 1.5.1 Isotropic spin exchange interactions

Isotropic Heisenberg interactions between spins of magnetic ions in insulators can be explained using the Hubbard model. The Hubbard model describes the behavior of electrons in a lattice of atoms with strong Coulomb interactions. For a pair of sites, the model can be equivalently represented as the problem of two quantum wells, expressed by

$$H_{\rm 2QW} = -t \sum_{\sigma=\uparrow,\downarrow} \left( c_{1,\sigma}^{\dagger} c_{2,\sigma} + c_{2,\sigma}^{\dagger} c_{1,\sigma} \right) + U \left( n_{1\uparrow} n_{1\downarrow} + n_{2\uparrow} n_{2\downarrow} \right). \tag{1.55}$$

In this equation, the first term describes the tunnelling between two sites (1 and 2) with a hopping amplitude $t > 0$. The operator $c_{i,\sigma}^{\dagger}$ ($c_{i,\sigma}$) creates (annihilates) an

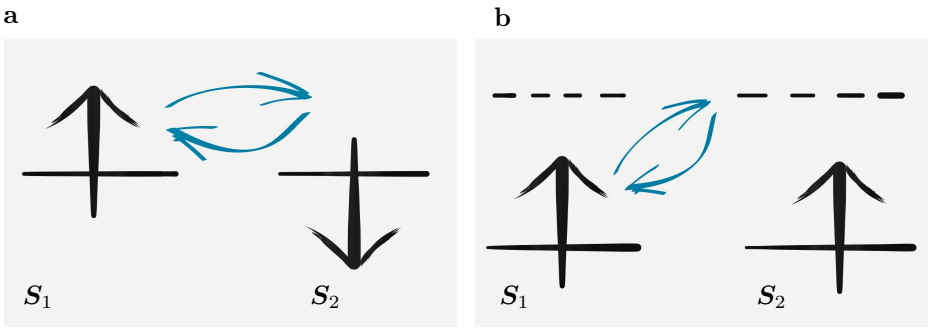


**Figure 1.7: Electron virtual exchange hopping.** **a** *Hopping between half-occupied sites* 1 *and* 2 *is allowed only for opposite spins due to the Pauli principle, leading to antiferromagnetic exchange interactions.* **b** *Hopping of electron from site* 1 *to an empty orbital on site* 2 *favors aligned spins* $\boldsymbol{S}_1$ *and* $\boldsymbol{S}_2$ *due to the Hund's rule coupling with the local spin on site 2, leading to ferromagnetic exchange interactions.*

electron with spin $\sigma =\uparrow,\downarrow$ on site $i = 1, 2$. The second term describes on-site Coulomb interactions that prevent double electron occupation ($U > 0$). The number of electrons is given by $n_{i,\sigma} = c^{\dagger}_{i,\sigma} c_{i,\sigma}$. Here, we use the tight-binding approximation, and the bound states of two quantum wells are the spherically-symmetric ($s$-type) localized atomic orbitals.

In the limit of strong on-site repulsion ($t << U$), two electrons become strongly localized on their respective sites. The spin degeneracy of such an insulating state is lifted due to the virtual electron delocalization, which can be described by second-order perturbation theory in $t$. This process is prohibited for parallel spins due to the Pauli principle. As a result, the electron delocalization reduces the energy of the state with antiparallel spin alignment (see Fig. 1.7 **a**) by an amount of $\Delta E = -\frac{2t^2}{U}$. The electron pair can be on either site 1 or 2 in the intermediate state, which gives the factor of two in the energy gain. One can additionally include off-diagonal hopping processes, which flip spins of two electrons, resulting in the Heisenberg exchange interaction:

$$H_{\text{ex}} = J\left(\mathbf{S}_1 \cdot \mathbf{S}_2 - \frac{1}{4}\right), \tag{1.56}$$

where $J = \frac{4t^2}{U}$ is the exchange interaction parameter, and $\mathbf{S}_i = \boldsymbol{\sigma}/2$ is the spin operator at site $i$, where $\boldsymbol{\sigma}$ is the vector of Pauli matrices. $J > 0$ favors antiparallel spin alignment, since the Hamiltonian becomes diagonal in the basis of the triplet and singlet spin states,

$$2\mathbf{S}_1 \cdot \mathbf{S}_2 = (\mathbf{S}_1 + \mathbf{S}_2)^2 - 2S(S+1), \tag{1.57}$$

and split their energy levels:

$$\langle \text{triplet}| H_{\text{ex}} |\text{triplet}\rangle - \langle \text{singlet}| H_{\text{ex}} |\text{singlet}\rangle = J. \tag{1.58}$$

Phenomenological Goodenough-Kanamori-Anderson (GKA) rules [53–55] predict spin-spin interactions in materials based on the occupancy of the overlapping ionic orbitals. The observation that the direct overlap between half-filled orbitals leads to strong antiferromagnetic interactions is often called the first GKA rule.

If we introduce a second empty orbital on each site, an additional hopping channel becomes possible when an electron from site 1 hops to the empty orbital on site 2. In this intermediate state, the Hund's rule coupling favors parallel spin alignment (see Fig. 1.7 **a**). These virtual processes promote ferromagnetism, and the effective Hamiltonian is

$$H_{\text{eff}} = \frac{-2t^2}{U - J_H(\boldsymbol{S}_1 \cdot \boldsymbol{S}_2)} \approx \frac{-2t^2}{U}(1 + \frac{J_H}{U}(\boldsymbol{S}_1 \cdot \boldsymbol{S}_2)) \tag{1.59}$$

This is often referred to as the second GKA rule, which states that effective hopping between an empty orbital of one ion and a filled orbital of another ion leads weak ferromagnetic interactions.

While the GKA empirical rules provide a simple and intuitive picture of magnetic interactions, a detailed analysis of all processes in the leading order of perturbation theory is necessary to understand these interactions in a specific material. Inter-orbital electron correlations are considered in the Extended Hubbard model:

$$H = -t \sum_{\langle i,j\rangle,\sigma} (c^{\dagger}_{i,\sigma} c_{j,\sigma} + \text{h.c.}) + U \sum_i n_{i\uparrow} n_{i\downarrow} + \sum_{i \neq j} V_{ij} n_i n_j, \tag{1.60}$$

In this model, intersite hopping amplitudes $t_{ij}$ are conveniently parametrized by Slater-Koster hopping integrals, describing $\pi, \sigma$ and $\delta$ hybridization between $s, p, d$ atomic orbitals. The electron pairwise interactions are described by Kanamori parameters [56]: two on-site Coulomb repulsion terms (single-orbital $U$ and inter-orbital $U'$) and the Hund's rule coupling ($J_{\text{H}}$). Intersite Coulomb interactions are not discussed in this thesis. The Extended Hubbard model encompasses a rich variety of phenomena, including Hubbard-Mott metal-insulator transitions, magnetic ordering, and superconductivity. It is a popular model for studies of strongly correlated many electron systems, and it has been used extensively in the field of high-temperature superconductivity.

The so-called *dp* model is widely used to describe magnetic materials. It is the Hubbard model that includes partially filled $d$ orbitals of magnetic transition metals and fully occupied $p$ orbitals of ligand ions. In most magnetic insulators, Anderson superexchange interaction [57] is the main source of interactions between magnetic ions. In this mechanism, an electron is virtually delocalized over the neighbor metal

site within the fourth-order perturbation theory in $pd$ hopping amplitudes $t_{pd}$. The energy decrease due to the delocalization is proportional to $-\frac{(t_{dd}^{\text{eff}})^2}{U}$, where $t_{dd}^{\text{eff}}$ is the effective $dd$ hopping amplitude expressed as $t_{dd}^{\text{eff}} = \frac{t_{dp}^2}{\Delta}$ with $\Delta$ being the energy to transfer the electron from a $d$ metal orbital to a $p$ ligand ion orbital. The effective $dd$ hopping amplitude is usually much larger than the $dd$ amplitude due to the direct overlap between $d$ orbitals of the two nearest metals. Superexchange is often called kinetic exchange, since it decreases the kinetic energy, i.e. enhanced electron delocalization causes its average momentum to decrease: $\Delta p \sim \frac{\hbar}{\Delta x}$. This iteraction conceptually differs from the direct Heisenberg exchange interaction, which is in essence the direct Coulomb exchange interaction $\sim \Psi_1^*(x)\Psi_2^*(x')\frac{e^2}{|x-x'|}\Psi_1(x')\Psi_2(x)$. Importantly, superexchange interactions depend on the energy of ligand ion states, which gives rise to spin-dependent $dd$ hoppings for ligand ions with large atomic numbers $Z$ having large SOC, e.g. iodine.

### 1.5.2 Anisotropic exchange interactions

The Dzyaloshinskii-Moriya interaction (DMI) is a type of anisotropic exchange interaction that arises due to the lack of inversion symmetry. It originates from the relativistic spin-orbit coupling, which couples the spin and momentum of electron. The DMI can be described as the antisymmetric part of the exchange interaction:

$$H_{\text{DMI}} = \sum_{i,j} \mathbf{D}_{ij} \cdot (\mathbf{S}_i \times \mathbf{S}_j), \tag{1.61}$$

where $\mathbf{D}_{ij}$ is the DMI vector that characterizes the strength and the form of the interaction between the spins on sites $i$ and $j$. The DMI vector strongly depends on the symmetry of the bond, in particular, on relative positions of the magnetic and ligand ions. In this section, we will calculate the DMI in the two anisotropic quantum wells model by including effects of SOC, which makes the hopping amplitudes in the Hamiltonian Eq. (1.55) spin-dependent:

$$H_{\text{a2QW}} = -\left(c_2^\dagger(t_0 + i\boldsymbol{t}_\lambda \cdot \hat{\boldsymbol{\sigma}})c_1 + \text{h.c.}\right) + U\left(n_{1\uparrow}n_{1\downarrow} + n_{2\uparrow}n_{2\downarrow}\right). \tag{1.62}$$

Here, we keep spin indices implicit, thus, $\hat{t} = (t_0 + i\boldsymbol{t}_\lambda \cdot \hat{\boldsymbol{\sigma}})$ is the matrix in spin space. $t_0$ is standard isotropic hopping amplitude, and $\boldsymbol{t}_\lambda$ encodes spin-dependent hopping due to SOC. The hopping Hamiltonian can be written as

$$-t\left(c_2^\dagger e^{i\phi \boldsymbol{n}\cdot\hat{\boldsymbol{\sigma}}} c_1 + \text{h.c.}\right), \tag{1.63}$$

where $t = \sqrt{t_0^2 + \boldsymbol{t}_\lambda^2}$, $\cos\phi = \frac{t_0}{t}$ ($\sin\phi = \frac{|\boldsymbol{t}_\lambda|}{t}$) and $\boldsymbol{n} = \frac{\boldsymbol{t}_\lambda}{|\boldsymbol{t}_\lambda|}$. By a rotation in spin space, the Hamiltonian can be transformed to the isotropic Hubbard model (see Eq. (1.55)):

$$c_1 = e^{-i\phi \boldsymbol{n}\cdot\hat{\boldsymbol{\sigma}}/2} c_1', \quad c_2 = e^{i\phi \boldsymbol{n}\cdot\hat{\boldsymbol{\sigma}}/2} c_2', \tag{1.64}$$

leading to the isotropic Heisenberg model in the rotated frame:

$$H_{\rm ex} = J\left(\mathbf{S}_1' \cdot \mathbf{S}_2' - \frac{1}{4}\right). \tag{1.65}$$

Here,

$$\begin{aligned} \mathbf{S}_1' &= \frac{1}{2} c_1'^{\dagger} \hat{\boldsymbol{\sigma}} c_1' = \frac{1}{2} c_1^{\dagger} \left(e^{-i\phi \boldsymbol{n}\cdot\hat{\boldsymbol{\sigma}}/2} \hat{\boldsymbol{\sigma}} e^{i\phi \boldsymbol{n}\cdot\hat{\boldsymbol{\sigma}}/2}\right) c_1, \\ \mathbf{S}_2' &= \frac{1}{2} c_2'^{\dagger} \hat{\boldsymbol{\sigma}} c_2' = \frac{1}{2} c_2^{\dagger} \left(e^{i\phi \boldsymbol{n}\cdot\hat{\boldsymbol{\sigma}}/2} \hat{\boldsymbol{\sigma}} e^{-i\phi \boldsymbol{n}\cdot\hat{\boldsymbol{\sigma}}/2}\right) c_2, \end{aligned} \tag{1.66}$$

Using this expression, we can rewrite Eq.(1.65) in the original spin basis. The spins in the rotated frame are expressed as

$$\boldsymbol{S}_1' = \begin{pmatrix} \cos\phi\, S_1^x + \sin\phi\, S_1^y \\ -\sin\phi\, S_1^x + \cos\phi\, S_1^y \\ S_1^z \end{pmatrix}, \quad \boldsymbol{S}_2' = \begin{pmatrix} \cos\phi\, S_2^x - \sin\phi\, S_2^y \\ \sin\phi\, S_2^x + \cos\phi\, S_2^y \\ S_2^z \end{pmatrix}, \tag{1.67}$$

if we introduce the $z$-axis in spin space to be parallel to the vector $\boldsymbol{n}$. Then, the scalar product of spins is

$$(\mathbf{S}_1' \cdot \mathbf{S}_2') = -\sin 2\phi \left[\boldsymbol{S}_1 \times \boldsymbol{S}_2\right]_z + \cos 2\phi\, (S_1^x S_2^x + S_1^y S_2^y) + S_1^z S_2^z, \tag{1.68}$$

which for an arbitrary spin quantization axis direction becomes

$$(\mathbf{S}_1' \cdot \mathbf{S}_2') = -\sin 2\phi\, \boldsymbol{n} \cdot \left[\boldsymbol{S}_1 \times \boldsymbol{S}_2\right] + \cos 2\phi\, (\boldsymbol{S}_1 \cdot \boldsymbol{S}_2) + (1 - \cos 2\phi)\, (\boldsymbol{S}_1 \cdot \boldsymbol{n})\, (\boldsymbol{S}_2 \cdot \boldsymbol{n}). \tag{1.69}$$

The resulting anisotropic spin model in the original spin basis is

$$\begin{aligned} H_{\rm ex} = \frac{4\left(t_0^2 - \boldsymbol{t}_\lambda^2\right)}{U} (\mathbf{S}_1 \cdot \mathbf{S}_2) - \frac{8 t_0 |\boldsymbol{t}_\lambda|}{U} \boldsymbol{n} \cdot \left[\boldsymbol{S}_1 \times \boldsymbol{S}_2\right] \\ + \frac{8\left(\boldsymbol{t}_\lambda\right)^2}{U} (\boldsymbol{S}_1 \cdot \boldsymbol{n})\, (\boldsymbol{S}_2 \cdot \boldsymbol{n}) - \frac{t_0^2 + \boldsymbol{t}_\lambda^2}{U}. \end{aligned} \tag{1.70}$$

The first term represents the modified isotropic Heisenberg exchange model. The second term of Eq. (1.70) is the asymmetric anisotropic DMI with the DMI vector given by

$$\boldsymbol{D}_{12} = -\frac{8 t_0 |\boldsymbol{t}_\lambda|}{U} \boldsymbol{n}. \tag{1.71}$$

This vector is of first order in the SOC strength $\lambda$, since $t_\lambda \sim \lambda$. Its directionality $\boldsymbol{n}$ is determined by bond symmetry. The third term is the symmetric anisotropic exchange of Ising type, proportional to $\lambda^2$. It is often referred to as Kitaev interaction, when the direction $\boldsymbol{n}$ varies for different bonds in the crystal.

### 1.5.3 Single-ion anisotropy

The single-ion anisotropy is a type of uniform magnetocrystalline anisotropy that arises from the anisotropic coupling between the magnetic moment of an atom and the crystal lattice. The coupling between the lattice and spin degrees of freedom is described by relativistic SOC

$$H_{LS} = \lambda \left( \boldsymbol{L}\boldsymbol{S} \right). \tag{1.72}$$

In insulators, the form of the single-ion anisotropy is dictated by symmetry of the ligand ions cage that coordinates the atom.

Drawing upon our calculation in the previous subsection, we can qualitatively understand the origin of the single-ion anisotropy, if we identify the states $|1\rangle$ and $|2\rangle$ in Eq. (1.62) with the two orbitals of the same site. In this case, the anisotropic hopping amplitude becomes effectively $i\boldsymbol{t}_\lambda = \lambda \langle 2| \boldsymbol{L} |1\rangle$ and $U$ plays a role of the energy difference between these two states. Then, using Eq. (1.70) with substitution $\boldsymbol{S}_1 = \boldsymbol{S}_2 = \boldsymbol{S}$, where $\boldsymbol{S}$ denotes the total spin of the ion, we obtain the expression for the single-ion anisotropy

$$H_{sia} = -\frac{8 \left( \boldsymbol{t}_\lambda \right)^2}{U} \left( \boldsymbol{S} \cdot \boldsymbol{n} \right)^2. \tag{1.73}$$

This single-ion anisotropy term favors the alignment of the spin along the axis $\boldsymbol{n}$ and is quadratic in the SOC strength. Such terms with the preferred axis $\boldsymbol{n}$ commonly arise in systems with tetragonal/orthorhombic ligand ion cages. In more symmetric cubic environments, the quadratic contribution becomes zero, and the leading order contribution is much smaller, being of the fourth order in the SOC.

## 1.6 Numerical methods

Soluble many-particle problems are limited to a number of celebrated cases, especially, for quantum spin systems, where the dimensionality of the spin space grows exponentially with the number of sites. We need to tailor our models, using effective models and semiclassical or classical approximations. These approximations are typically suitable for the time, length and energy scales that we are interested in. It is essential to tailor numerical methods for energy optimization to find accurate phase diagrams, for studying dynamics of these many-body systems and for simulating their collective response to external driving forces. In this section, we discuss numerical approaches that are used in the thesis to address these challenges.

### 1.6.1 Landau-Lifshitz-Gilbert equation for Heisenberg spins

The Landau-Lifshitz-Gilbert (LLG) equation is commonly used for simulating the dynamics of Heisenberg spins in magnetic materials. It describes the time evolution

of the unit vector along the magnetization $\mathbf{m}_n$ on a lattice site $n$, and includes the effects of damping. The LLG equation is

$$\frac{\partial \mathbf{m}_n}{\partial t} = \gamma \mathbf{h}_n^{\text{eff}} \times \mathbf{m}_n + \alpha \mathbf{m}_n \times \frac{\partial \mathbf{m}_n}{\partial t}, \tag{1.74}$$

where $\gamma > 0$ is the gyromagnetic ratio, $\mathbf{h}_n^{\text{eff}} = -\frac{\partial E}{\partial \boldsymbol{m}_n}$ is the effective magnetic field on site $n$, $\alpha > 0$ is the dimensionless Gilbert damping coefficient. The first term in the right-hand side of the equation represents the precession of the magnetization around the effective magnetic field, while the second term represents the damping of the magnetization. At a nonzero temperature, the equation is supplemented with a stochastic magnetic field.

The LLG equation is a classical equation of motion that can be derived from the Heisenberg model, which describes the interaction between magnetic moments of individual atoms. It represents a set of coupled differential equations that can be solved numerically using a variety of methods, including finite-difference integration methods. It is also effectively used to simulate continuum micromagnetic and effective models and find their minima energy configurations, which are discretized by using the finite-element method.

### 1.6.2 Glauber dynamics for Ising spins

The Glauber dynamics is a powerful tool for studying the equilibrium and non-equilibrium behavior of spin systems. It is a Monte Carlo algorithm used for simulating the time evolution of classical spin systems, such as the Ising model. In the Glauber dynamics, the system evolves through a sequence of discrete time steps, where at each step, a randomly selected spin is flipped with a probability:

$$P(\Delta E) = \frac{1}{1 + \exp(-\Delta E/T)}, \tag{1.75}$$

where $\Delta E$ is the system energy change after flipping the spin, and $T$ is the temperature.

### 1.6.3 Stochastic gradient energy optimization

The Stochastic Gradient Descent (SGD) algorithm is an efficient method for minimizing energy when the energy can be represented as a functional $E[X_i]$, where $X_i$ is a set of constrained scalar functions. For example, in a ferromagnet, $X_i$ could represent the amplitudes of $N$ Fourier harmonics of magnetization. At each step, the set of $X_i$ is updated using the gradient descent:

$$X_i \to X_i - \eta \frac{\partial E[X_j]}{\partial X_i} \tag{1.76}$$

Here, $\eta > 0$ (known as the learning rate) is initially set to a small and increased if the energy decreases after the update. The SGD algorithm additionally includes repeating the set of gradient descent updates with an additional disorder in the configuration in the first step. The strength of the disorder gradually decreases in order to reach the energy minimum. To handle complex energy landscapes, the initial strength of the disorder can be adapted, allowing the system to overcome large energy barriers between different local energy minima. The SGD methods can be complemented with more accurate but also slow non-gradient energy optimization techniques, which are also widely used and can be found in the *fminsearch* method implemented in MATLAB.

## 1.7 Thesis outline

The rest of the thesis is organized as follows.

**In Chapter 2**, we study magnetic bubbles with Skyrmion topology induced by the interaction between magnetic dipoles in a magnetic model with realistic parameters describing thin film itinerant ferromagnet, $SrRuO_3$. This material shows unprecedented stability of the Skyrmion crystal to temperature variations and tilted applied magnetic fields. The interplay between the magnetostatic, second- and fourth-order anisotropic interactions was found to be crucial in describing this robust Skyrmion crystal phase. In addition, we discuss effects of interfacial DMI on magnetic phases of this material.

**In Chapter 3**, we predict 3D Skyrmions in the Fe-based langasite, $Ba_3TaFe_3Si_2O_{14}$. We propose an effective model describing large scale magnetic superstructures in this material, which reproduces recent experimental data. We calculate phase diagrams of this model in applied magnetic fields. We find novel magnetic states, such as two-dimensional vortex arrays, as well as individual vortices, including a novel coreless vortex with a finite energy. The energy divergence of two-dimensional Skyrmions in the model was explained using an analogy with electrostatic interactions. The predicted novel 3D Skyrmion bears close resemblance to the Skyrmion predicted to describe baryonic matter in particle physics and predicted 3D Shankar soliton in superfluid $A$ phase of $^3$He.

**In Chapter 4**, we derive the anisotropic $JK\Gamma$ effective spin model of $CrI_3$ ferromagnetic van der Waals material, starting from the microscopic $dp$ model. The effective model includes the isotropic Heisenberg interaction $\sim J\left(\boldsymbol{S}_1 \cdot \boldsymbol{S}_2\right)$, Kitaev interaction $\sim K\left(S_1^z S_2^z\right)$ (bond-dependent Ising interaction) and the off-diagonal $\sim \Gamma(S_1^x S_2^y + S_1^y S_2^x)$ exchange interactions. Our calculations included the strong on-site Coulomb repulsion, Hund's rule coupling, the spin-orbit coupling on I ions and the hopping between the ligand ions. The interactions between nearest-neighbor Cr ions were calculated in the fourth-order of perturbation theory in the virtual electron

hopping between the $p$ orbitals of I and the $d$ orbitals of Cr ions. The spin-orbit coupling on ligand ions leads to exchange energy anisotropy described by the $K$ and $\Gamma$ terms. We developed a procedure to calculate the effective spin-dependent hopping amplitudes for arbitrarily separated Cr ions. Detailed symmetry analysis was performed to support the direct calculations. We compute magnon spectra for calculated interactions, which helps to restrict parameters of the model.

**In Chapter 5**, we numerically study the magnetization reversal process in a chiral ferrimagnetic material, which is both multiferroic and magnetoelectric. Our simulations explain the recently observed humps of electric polarization in the magnetic switching process of the Zn-doped kamiokite $Fe_{2-x}Zn_xMo_3O_8$. Surprisingly, the electric polarization peaks originate from the metastable antiferromagnetic phase intervening between the magnetization up and down states.